IJMMM International Journal of Minerals, Metallurgy and Materials 矿物冶金与材料学报（英文版）

# $Al^{3+}$ doped $CeO_2$ for proton conducting fuel cells

Sarfraz, Shahzad Rasool, Muhammad Khalid, M.A.K. Yousaf Shah, Bin Zhu, Jung-Sik Kim, Muhammad Imran Asghar, Nabeela Akbar, and Wenjing Dong

Cite this article as:
Sarfraz, Shahzad Rasool, Muhammad Khalid, M.A.K. Yousaf Shah, Bin Zhu, Jung-Sik Kim, Muhammad Imran Asghar, Nabeela Akbar, and Wenjing Dong, $Al^{3+}$ doped $CeO_2$ for proton conducting fuel cells, *Int. J. Miner. Metall. Mater.*, 31(2024), No. 10, pp. 2253-2262. https://doi.org/10.1007/s12613-024-2910-z

View the article online at SpringerLink or IJMMM Webpage.

---

INTERNATIONAL JOURNAL OF
Minerals, Metallurgy and Materials

*Volume 31, Number 10, October 2024*
*Page 2253*

Research Article https://doi.org/10.1007/s12613-024-2910-z

# $Al^{3+}$ doped $CeO_2$ for proton conducting fuel cells

*Sarfraz*[1)], *Shahzad Rasool*[1)], *Muhammad Khalid*[1)], *M.A.K. Yousaf Shah*[1)], *Bin Zhu*[1),✉], *Jung-Sik Kim*[3)], *Muhammad Imran Asghar*[4)], *Nabeela Akbar*[1),✉], *and Wenjing Dong*[2),✉]

1) Jiangsu Provincial Key Laboratory of Solar Energy Science and Technology/Energy Storage joint Research Center, School of Energy and Environment, Southeast University, Nanjing 210096, China

2) School of Microelectronics, Hubei University, Wuhan 430062, China

3) Sino-French Engineer School/School of General Engineering, Beihang University, Beijing 100191, China

4) Renewable Energy Technologies Group, Faculty of Engineering and Natural Sciences, Tampere University, FI-33014, Finland

(Received: 13 December 2023; revised: 4 April 2024; accepted: 15 April 2024)

**Abstract:** Developing high ionic conducting electrolytes is crucial for applying proton-conducting fuel cell (PCFCs) practically. The current study investigates the effect of alumina on the structural, morphological, electrical, and electrochemical properties of $CeO_2$. Lattice oxygen vacancies are induced in $CeO_2$ by a general doping concept that enables fast ionic conduction at low-temperature ranges (300–500°C) for PCFCs. Rietveld refinement of the X-ray diffraction (XRD) patterns established the pure cubic fluorite structure of Al-doped $CeO_2$ (ADC) samples and confirmed Al ions' fruitful integration in the $CeO_2$ lattice. The electronic structure of the alumina-doped ceria of the materials (10ADC, 20ADC, and 30ADC) has been investigated. As a result, it was found that the best composition of 30ADC-based electrolytes induced maximum lattice oxygen vacancies. The corresponding PCFC exhibited a maximum power output of 923 mW/cm$^2$ at 500°C. Moreover, the investigation proves the proton-conducting ability of alumina-doped ceria-based fuel cells by using an oxide ion-blocking layer.

**Keywords:** proton ceramic fuel cells; oxygen vacancies; higher fuel cell performance; doping; fast ions transportation

## 1. Introduction

Proton-conducting fuel cells (PCFCs) offer a promising solution for efficient and environmentally friendly energy conversion, specifically at low operating range, i.e., around 550°C. High proton conducting electrolytes with thermally and electrochemically compatible electrodes are in great need for realizing highly efficient PCFCs. Barium cerite and barium zirconate based on perovskite oxides are commonly used as proton-conducting ceramics. However, their protonic conductivities and overall performances are still behind when compared with conventional high-temperature fuel cells, e.g., using yttria-stabilized zirconia (YSZ) [1–4]. In the aspect of ionic conductivity, interpretation of semiconductor electrochemistry is required in order to develop semiconductor ionic materials with advanced high proton conductivities that can replace those perovskite proton electrolytes in low-temperature operating PCFCs [5–7]. Recently, it has been reported that proton conduction character and resulting conductivity can be tuned in via surface engineering by accomplishing a core–shell structure and through surface doping in some oxide ceramic materials, e.g., $CeO_2$, that lead to a noticeably high proton conductivity of ~0.1 S/cm at 550°C [8–11]. Additionally, high-performance operation with optimum ionic conductivity and long-term stability at low operating temperature (450–550°C) has been realized by the use of semiconductor-based materials such as gallium doped ceria (GDC) and other single-layer electrolytes [12–13]. In particular, a GDC nanocrystalline electrolyte with high ionic conductivity of 0.37 S/cm and excellent fuel cell performance of 591 mW/cm$^2$ at 550°C has been found by Chen *et al.* [14]. Shah *et al.* [15] investigated GDC electrolyte shows a power density of 569 mW/cm$^2$ with a maximum ionic conductivity of 0.1 S/cm even at 450°C. The Li-based metal oxide layered structure $Ni_{0.8}Co_{0.15}Al_{0.05}LiO_{2-\delta}$ (NCAL) has been widely utilized as electrode materials in semiconductor-based fuel because of its superior redox reaction rate and excellent catalytic activity at low operating temperatures (300–600°C) [16]. Additionally, a variety of doped ceria-based semiconductors and ionic conducting electrolytes (single-phase) have been established for their excellent power density and stability at low (450–550°C) and intermediate (500–650°C) temperatures [17–20].

The electrolyte materials play a crucial role in facilitating proton transport within a cell, and cerium dioxide ($CeO_2$), known as ceria, has become an emerged material for such in-

✉ Corresponding authors: Bin Zhu E-mail: zhu-bin@seu.edu.cn; Nabeela Akbar E-mail: nabeela4426@gmail.com; Wenjing Dong E-mail: wenjingd@hubu.edu.cn

vestigations as a potential proton conductor due to its ability to modulate oxygen vacancies and introduce proton conduction at elevated temperatures (300–500°C) for PCFCs. Aluminum oxide ($Al_2O_3$), also known as alumina, is used in various applications such as photocatalysts, sensors, electronics, optical, magnetic, coating, and as a catalyst due to its high surface area, thermally stable, and high mechanical resistance [21–24]. Alumina is emerging as a tremendous potential and novel material to create surface defects to tune the inherent oxygen vacancies, which boost the ionic conductivity [25].

Here, we present a new approach to tune inherent oxygen vacancies into proton carriers and develop proton conduction for high-performance Al–$CeO_2$-based PCFCs. Specifically, we explore the incorporation of low-valency cations, particularly $Al^{3+}$, into $CeO_2$ to promote oxygen vacancy concentration and, importantly, establish surface and bulk doping gradients to create local concentration gradience for enhanced proton transport.

## 2. Experimental

### 2.1. Synthesis of alumina doped ceria (ADC) powder

All the chemicals used in this investigation were commercially available, analytical-grade products from Sinopharm Chemical Reagent Co., Ltd. in China. They were utilized precisely as received, requiring no further purification steps. The proton conducting electrolyte materials $Al_xCe_{1-x}O_2$ (where $x$ = 0.1, 0.2, and 0.3) as alumina doped ceria (ADC) were prepared via a direct sintering method. Calculated amounts of cerium nitrate and aluminum nitrate with varying contents were dissolved in 20 mL of deionized water. The solution was dried in a digital oven at 120°C for 24 h. The dried material was ground well to make it a fine powder. Afterwards, the powder was calcinated in a muffle furnace at 1000°C for 4 h to acquire the final product, denoted as ADC. Three types of ADC with various amounts of alumina (10mol%, 20mol%, and 30mol%) and ceria were denoted as 10ADC, 20ADC, and 30ADC.

Commercially available nickel cobalt aluminum lithium oxides ($Ni_{0.8}Co_{0.15}Al_{0.05}LiO_{2-\delta}$, NCAL), purchased from Tianjin Bamo Sci. & Tech. Joint Stock Ltd., China, has been used as the symmetrical electrodes, catalyst, and current collectors. The NCAL–Ni electrodes were made using a terpinol solvent and commercial NCAL powders. The NCAL powder was mixed with the necessary amount of terpinol to attain the viscous paste of NCAL electrodes. However, Ni-foam in the form of a button was also cut simultaneously, having 0.64 $cm^2$ of the active area. A thick slurry was applied to the Ni-foam and allowed to dry for 20 min at 120°C to make the NCAL–Ni electrodes.

### 2.2. Fuel cell configuration and evaluation

The prepared ADC-based electrolyte materials were compressed and placed between two symmetric NCAL–Ni electrodes. Inserted NCAL Ni-foams serve as symmetrical electrodes, while ADC is an electrolyte. Later, the electrodes and electrolytes (where the electrolyte was sandwiched between the symmetrical electrodes) were placed in a die and compressed at 250 MPa for 2 min to produce a button-shaped pellet with an active area of 0.64 $cm^2$ and a diameter of 13 mm. The electrolyte in the cell was approximately 0.65 mm thick, whereas the produced pellet had a thickness of 1.5 mm. Two hours before the fuel cell performance test, the prepared cell with the following configuration (NCAL–Ni/ADC/Ni–NCAL) was sintered at 550°C. Afterwards, the cell was inserted into the apparatus to begin electrochemical impedance spectroscopy (EIS) and fuel cell performance measurements. Pure hydrogen was provided as fuel on the anode side and air as an oxidant on the cathode side at rates of 90–120 mL/min and 160–200 mL/min, correspondingly. A programmable electronic load (IT8511A) was used to measure voltage and current and plot the characteristic curves for current–voltage ($I$–$V$) and current–power ($I$–$P$) to study the fuel cell performances. The electrochemical workstation Energy Lab XM was utilized to determine the EIS in an $H_2$/air atmosphere at various operating temperatures ranging from 380 to 500°C. For this measurement, the applied frequency range was 0.1 Hz–1 MHz with an amplitude of 10 mV.

2.2.1. Hydrogen concentration cell and oxygen concentration cell

The 30ADC material was pressed into a circular disc with a diameter of 13 mm by using a hydraulic press under pressure of 450 MPa. To prepare the fuel cell devices, silver paste was pasted on both sides of the disc and allow it to dry. The cell devices that use 30ADC as electrolytes are preheated for 2 h at 550°C. Next, the temperature was dropped to 420°C. Then, the anode and cathode of the cell were treated with 99.999% pure $H_2$ and 5% $H_2$/Ar. Heating at intervals of 20°C was used to measure open circuit voltage (OCV) to 560°C. The atmosphere on both sides of the oxygen concentration cell was then replaced with air and 2% $O_2$/Ar to determine the oxygen concentration.

2.2.2. Characterization techniques

Several characterization techniques are used to evaluate the effect of $Al^{3+}$ doping in $CeO_2$. X-ray diffraction (XRD) is employed to analyze doping-induced structural changes, providing insights into the altered crystal structure and phase composition. Further, the Rietveld refinement profile of XRD patterns is performed for phase purification utilizing the FULLPROF program. Moreover, high-resolution transmission electron microscopy (HR-TEM) and scanning electron microscopy (SEM) offer comprehensive details regarding the distribution, size, and shape of the doped $CeO_2$ particles throughout the samples. Raman spectroscopy elucidates the lattice distortions induced by $Al^{3+}$ substitution by investigating the vibrational modes of the doped material. X-ray photoelectron spectroscopy (XPS, Thermo Scientific K-Alpha) assessed the surface properties of powdered 10ADC, 20ADC, and 30ADC. To describe the proton conduction behavior in the samples, EIS is utilized. An analysis technique called DRT converts impedance data as a function of frequency in-

to a distribution of the system's time constants. By applying the distribution of relaxation time (DRT) approach to EIS analysis, it is possible to obtain a high-resolution identification of the polarization processes. As a result, the DRT curve makes it possible to distinguish between the polarization processes that overlap in the EIS curve.

In order to achieve the attractive cell's performance, it is crucial to determine the optimal concentration of $Al^{3+}$ doping in $CeO_2$. The realistic effect of different doping levels (10mol%, 20mol%, and 30mol%) on the oxygen vacancy concentration and proton conductivity was examined. Simultaneously, surface and bulk doping techniques need to be developed and optimized to establish the desired concentration gradients. It is essential to strike a balance between oxygen vacancy formation, structural integrity, and surface properties to determine the optimum $Al^{3+}$ doping concentration.

## 3. Results and discussion

### 3.1. Structural and phase analysis

The room temperature XRD pattern and Rietveld refinement patterns of prepared ADC electrolyte powder with different contents via direct sintering route are shown in Fig. 1. The XRD patterns shown in Fig. 1(a) for the ADC samples sintered at 1000°C for 4 h confirm the cubic fluorite structure (JCPDS no. 43-1002) with space group $Fm\bar{3}m$. It can be signified that all the characteristic peaks belong to the cubic phase of pure ceria, with no secondary phase identified in the XRD pattern; it is advised successful doping of alumina in ceria [26–29]. Reduction in the most intense peak (111) is due to the $Al^{3+}$ substitutions at $Ce^{4+}$ sites, leading to the significant lattice expansion [30]. Because the ionic radius of aluminum is smaller than that of cerium, when aluminum ions replace cerium ions in the ceria lattice, the smaller size of aluminum ions can cause distortion in the local lattice. As a result of aluminum incorporation, there is an elevation in lattice parameters. The rise in lattice parameters, attributed to aluminum doping, leads to a displacement of XRD peaks toward lower diffraction angles. This shift occurs due to the increased interplanar spacing resulting from the expanded lattice. From Rietveld refinement patterns, as shown in Fig. 1(b)–(d), the investigation demonstrates that Al doping in $CeO_2$ has no effect on the cubic fluorite structure of $CeO_2$, further supporting the idea that Al-doped $CeO_2$ lattice only forms a single cubic phase. Moreover, the unit cell volume, lattice parameter, and consistency factors like reliability factor (*R*-factor), profile *R*-factor ($R_p$), weighted profile *R*-factor ($R_{wp}$), expected *R*-factor ($R_{exp}$), and Bragg *R*-factor ($R_{Bragg}$) are the best-fitted values as listed in Table 1. Most of the alumina take the interstitial lattice sites of the ceria lattice or stay at the grain boundaries to stabilize the structure. However, doped alumina leads to change in the lattice parameter and unit cell volume of the host material because of the smaller radius of $Al^{3+}$ ions (0.57 Å) than that of $Ce^{4+}$ ions (0.92 Å). The variation in lattice parameter can certainly induce defects such as oxygen vacancies on the lattice sites.

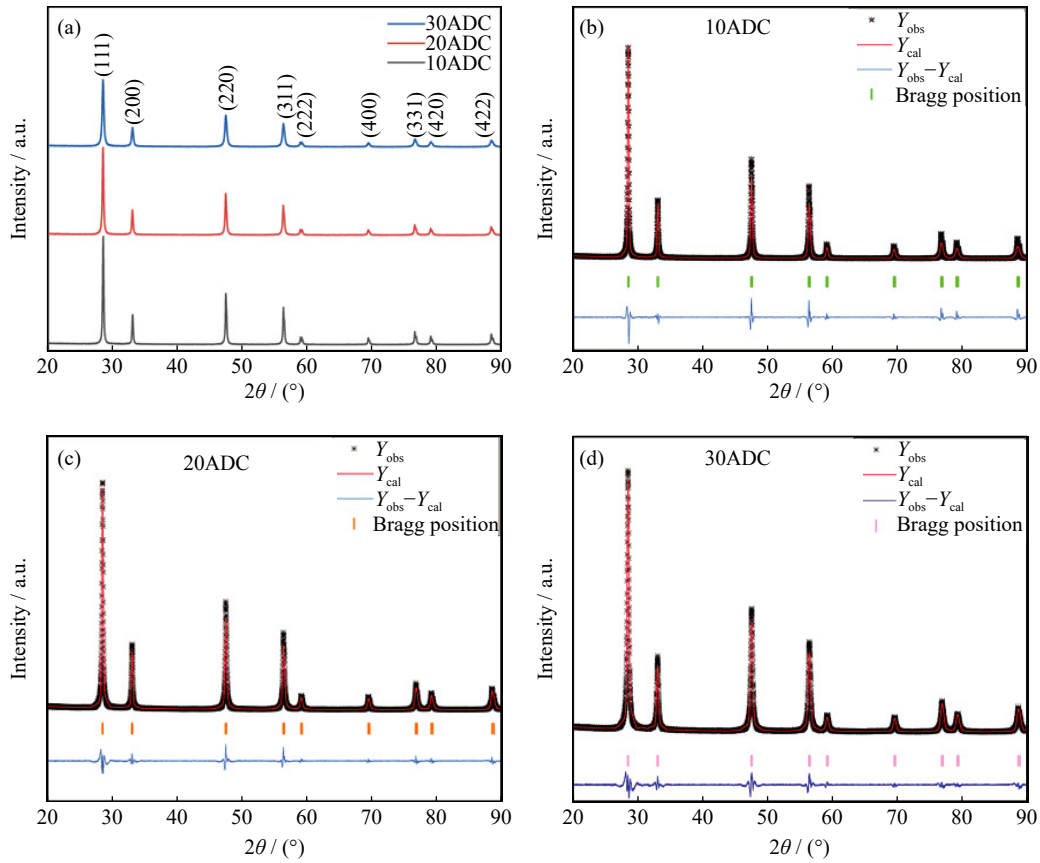


**Fig. 1. Microstructural analysis: (a) XRD pattern of Al–$CeO_2$ with different contents; (b–d) Rietveld refined patterns of 10ADC, 20ADC, and 30ADC, respectively. $Y_{obs}$ and $Y_{cal}$ are the observed data and calculated data, respectively.**

**Table 1. Lattice parameters, average crystallite size, and Rietveld refinement results profile of Al-doped $CeO_2$ with different compositions**

| Composition | Lattice parameter / Å | Average crystallite size / nm | Unit cell volume / Å$^3$ | *R*-factor | $R_p$ | $R_{wp}$ | $R_{exp}$ | $R_{Bragg}$ |
|---|---|---|---|---|---|---|---|---|
| $Al_{0.1}Ce_{0.9}O_2$ | 5.4083 | 30 | 158.25 | 0.531 | 14.6 | 17.4 | 13.17 | 0.893 |
| $Al_{0.2}Ce_{0.8}O_2$ | 5.4113 | 26 | 158.46 | 0.585 | 21.2 | 23.5 | 13.9 | 1.109 |
| $Al_{0.3}Ce_{0.7}O_2$ | 5.4118 | 21 | 159.28 | 0.729 | 21.4 | 26.8 | 15.4 | 1.150 |

### 3.2. Morphological analysis

SEM and HR-TEM are conducted to inspect the microstructure and morphology of Al–$CeO_2$ as represented in Fig. 2. Two SEM images (Fig. 2(a) and (b)) and two HR-TEM images (Fig. 2(g) and (h)) at varying resolution illustrate its small and uniform distribution of nano-level particles. Many acquaintances developed between these grains or particles. Also, these results demonstrate that Al considerably expands the lattice planes of the crystalline phase of ceria, correlating the lattice parameter difference seen above in XRD and proving the incorporation of alumina in the ceria lattice. Additionally, the 10 nm HR-TEM image shows the development of a surface layer with increased oxygen vacancies, which facilitates charge transmission. The HR-TEM picture was enlarged using the ImageJ software to clearly show the plane (220) with an interplanar *d*-spacing of 0.21 nm, as shown in Fig. 2(h). However, the presence of alumina is visible and measured in element mapping images of Fig. 2(c)–(f). Even though certain regions are more Al–rich than ceria, the Al and $CeO_2$ mappings show a somewhat homogeneous mixing of the two elements. As a result, Al incorporation into the $CeO_2$ lattice is confirmed by the diffraction and microscopy results of Al–$CeO_2$ nanoparticles. The obtained nanostructure benefits from the synergistic effects of the characteristics of the 30Al–$CeO_2$ particles, which benefits the constructed device's electrochemical properties. The formation of nanoparticles of ADC manifests the increased surface area, which enables and creates more active sites and improves the performance of the structured fuel cell device.

### 3.3. Raman spectra and XPS analysis

Raman spectroscopy is a scientific technique used to determine molecules' vibrational and rotational modes. Fig. 3(a) shows Raman spectra of ADC with different Al-dopant contents. The high-intensity peak at 462 cm$^{-1}$ is attributed to $F_{2g}$ mode of $CeO_2$ [31–33]. Phonon confinement, stress, and enlargement associated with size defects, distribution, and variations in phonon relaxation with particle size are some reasons that cause the Raman peak position of 462 cm$^{-1}$ peak to fluctuate due to doping [34]. The Al-doping may induce local structural changes or distortions in the ceria lattice. These structural modifications could affect the Raman scattering behavior of the material. Depending on the dopant

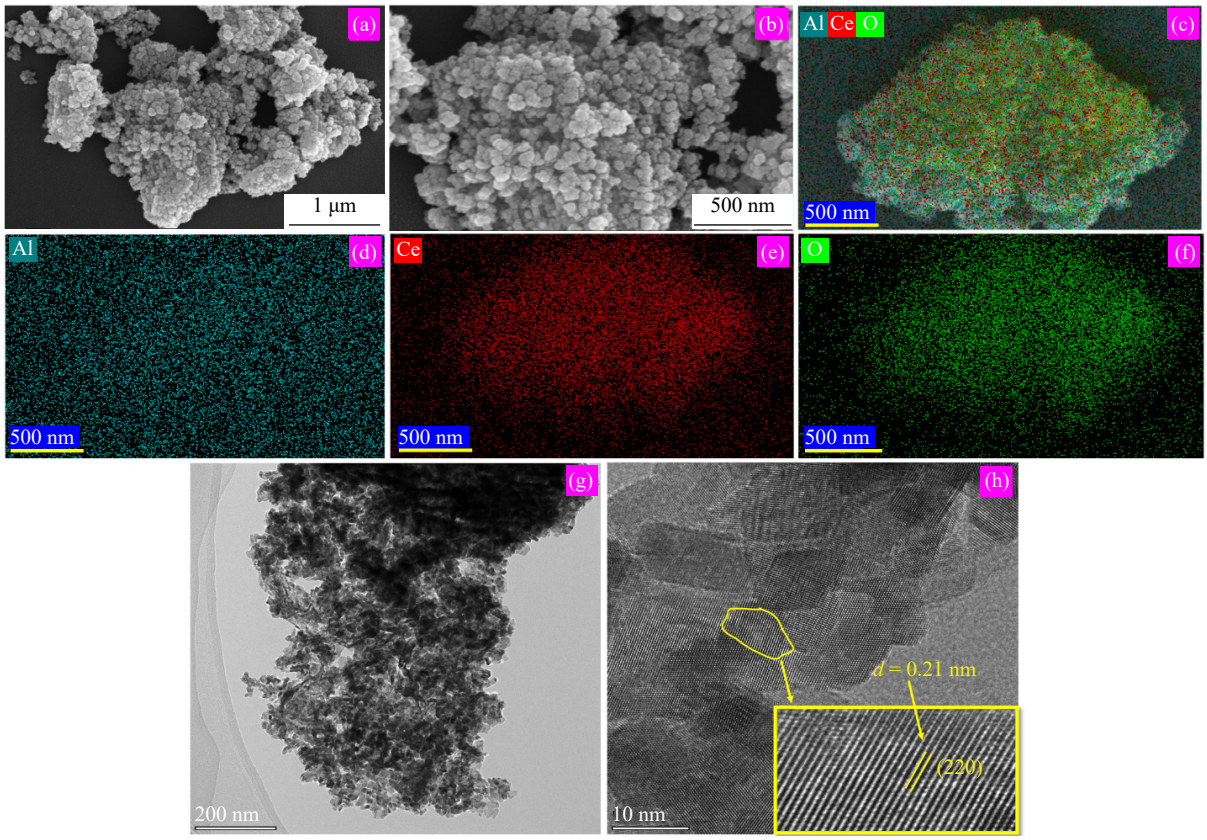


**Fig. 2. (a, b) Morphological characterization and SEM images, (c–f) element mapping images, and (g, h) HR-TEM images of 30ADC powder.**

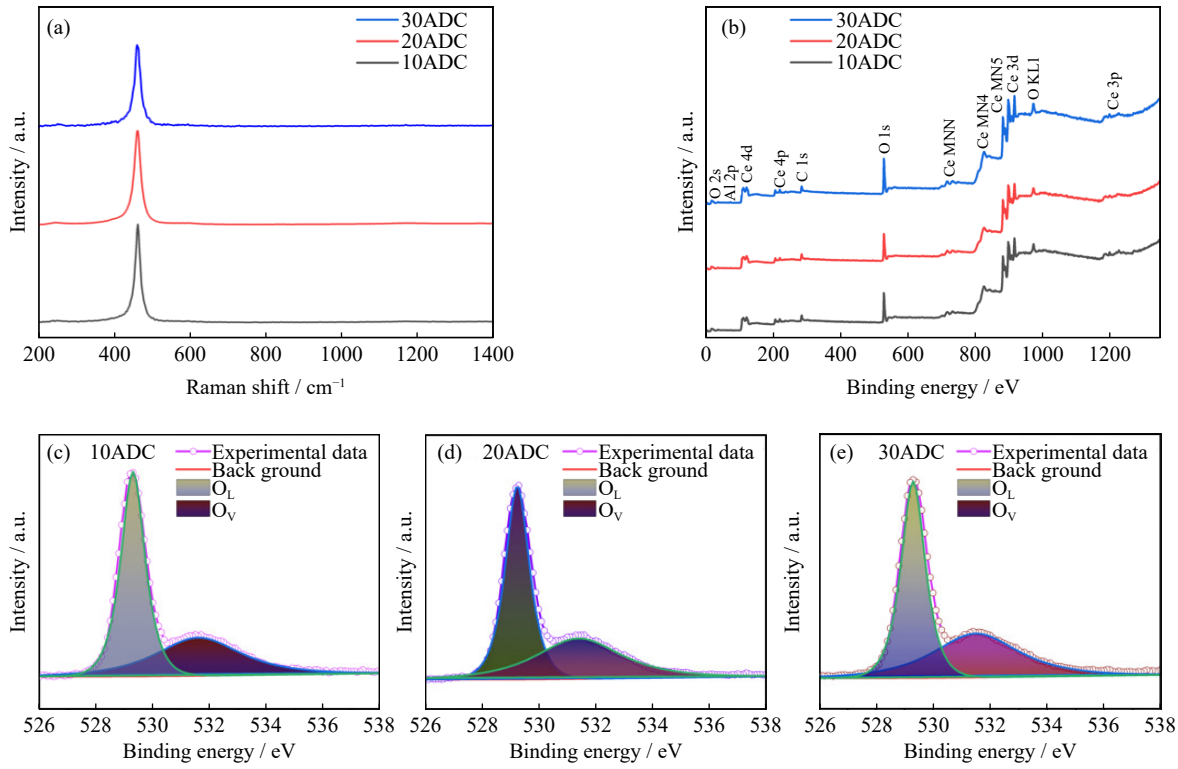


**Fig. 3. (a) Raman analysis, (b) XPS survey spectra, and (c–e) O 1s spectra of Al–$CeO_2$ with different contents.**

content and synthesis conditions, there might be a possibility of phase segregation, where certain material regions have a different composition or structure. This phase separation could influence the Raman spectra.

XPS is employed to investigate the surface properties, such as the creation of defects and the chemical composition of the prepared electrolyte materials. Fig. 3(b) shows the XPS survey spectra of 10ADC, 20ADC, and 30ADC. The XPS survey spectra of Al-doped $CeO_2$ with different concentrations confirm the occurrence of Al, Ce, and O elements in the materials. XPS spectra of the O 1s area are utilized to provide more information about the surface hydroxyl group ($OH^-$), lattice oxygen, absorbed oxygen, and oxygen vacancies [35–36]. The O 1s scan of 10ADC, 20ADC, and 30ADC provides evidence of the lattice oxygen and oxygen vacancies, as shown in Fig. 3(c)–(e). The peak at lower binding energy, 529.3 eV, may be attributed to lattice oxygen species ($O_L$), whereas the peak at higher binding energy, 531.2 eV, may be attributed to oxygen defects ($O_V$) [37–38]. Additionally, the development of oxygen vacancies is represented by the area ratio of the peak oxygen defects to the peak oxygen lattice ($O_V/O_L$). The relative area ratio values for the 10ADC, 20ADC, and 30ADC are calculated to be 0.62, 0.78, and 0.84, respectively. It can be indicated that more incorporation of alumina contents in ceria induces the more oxygen vacancies. The enhanced oxygen vacancies, to a certain extent withing the tested range, increase proton conduction as a result of the cell's rapid catalytic activity, which will significantly enhance electrochemical performance.

### 3.4. Electrochemical performance test

The *I–P* and *I–V* characteristic curves at low temperature ranges (380–500°C) are indicated as in Fig. 4 to determine the fuel cell performance of ADC based electrolytes using hydrogen as a fuel and oxygen as an oxidant. NCAL was chosen as a result of its rapid catalytic reactions for oxygen reduction (ORR) and hydrogen oxidation (HOR). Employing NCAL–Ni/ADC/Ni–NCAL configuration, high power output and open circuit voltage (OCV) of the fuel cell were taken into account when evaluating its performance. As long as the fuel cell maintained a steady OCV, its performance was evaluated. Fig. 4(a) represents the comparison of electrochemical performances of 10ADC, 20ADC, and 30ADC based electrolytes, exhibiting peak power densities of 765, 859, and 923 mW/cm$^2$ respectively at an operating temperature of 500°C. After conducting the tests for electrochemical performance, it was revealed that 30ADC performed the best among the others and achieved a maximum power density of 923 mW/cm$^2$ at 500°C when stable OCV was 1.077 V, while pure $CeO_2$ reported 533 and 515 mW/cm$^2$ at 550 and 510°C, and even has low fuel cell performance at higher temperature as compared to ADC materials [39–40]. Additionally, the peak power densities of 30mol% Al doped $CeO_2$ based cell as represented in Fig. 4(b) influence 923, 857, 628, 424, and 205 mW/cm$^2$ at an operational temperature of 500, 470, 440, 410, and 380°C, respectively. The maximum power output initially enhanced with the influence of alumina contents. The performance of NCAL–Ni/30ADC/NCAL–Ni configuration at 500°C was significantly greater than that from reported pure or doped $CeO_2$ [14,41–45]. Hence, the experimental results showed that the cell performance had improved, primarily as a result of increased ionic conductivity and oxygen vacancies. These factors are crucial for enhancing the electrochemical performances of the electrolyte and facilitat-

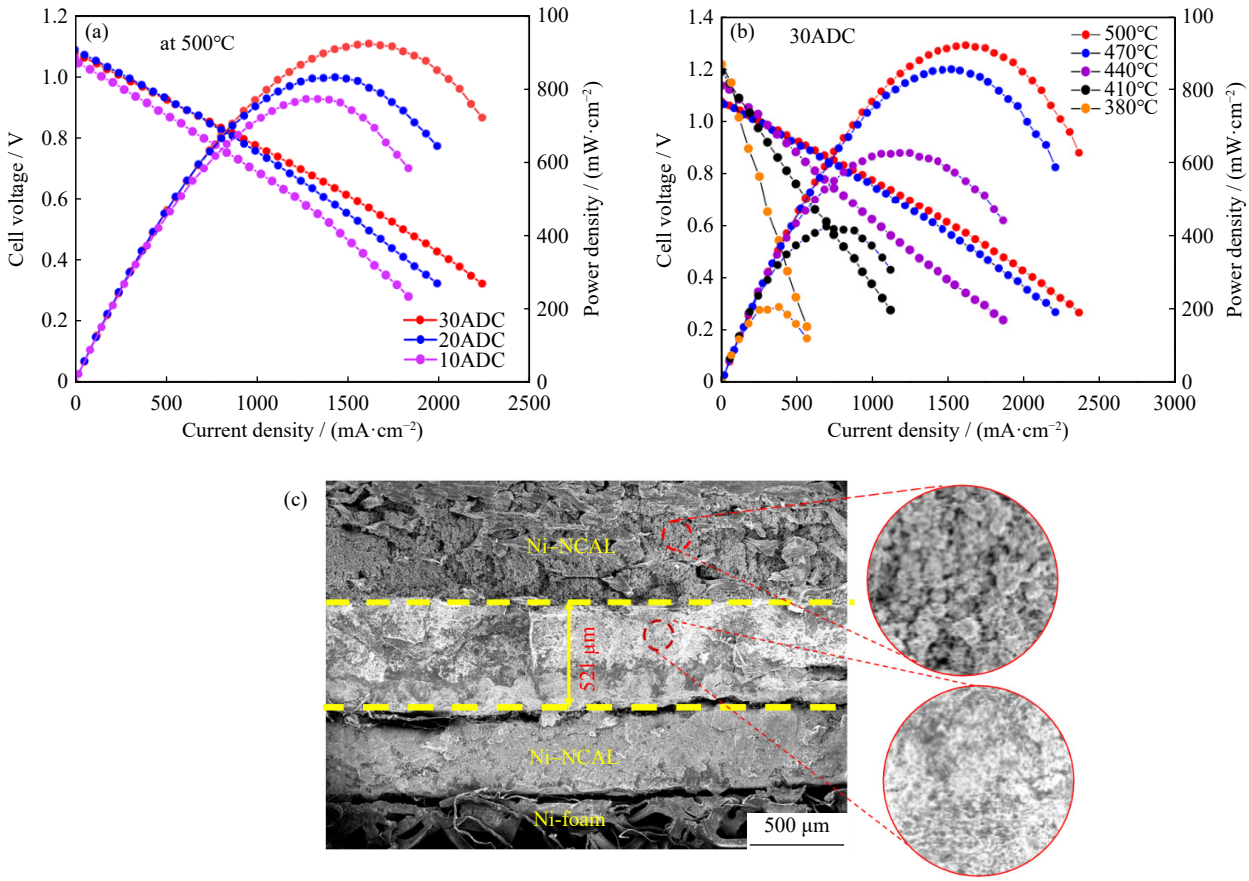


**Fig. 4.** ***I–P*** **and** ***I–V*** **characteristics curves: (a) fuel cell performances comparison of 10ADC, 20ADC, and 30ADC as electrolytes at 500°C; (b) best fuel cell device (Ni–NCAL/30ADC/NCAL–Ni) under different operating temperature. (c) Cross-sectional SEM view of 30ADC after test.**

ing rapid ionic transport. A cross-sectional SEM image of 30ADC cell is shown in Fig. 4(c) after fuel cell performance test, where the three layers of relatively dense electrolyte with thickness of 521 μm and porous electrodes are exhibited.

### 3.5. EIS and DRT analysis

To explore the electrochemical characteristics of PCFCs based on 10ADC, 20ADC, and 30ADC electrolytes, EIS was carried out from the same cell of Fig. 4(a) and (b). As illustrated in Fig. 5(a), EIS comparison spectra were measured at 500°C, a temperature similar to that of fuel cell environment. With a 10 mV AC signal applied, the EIS spectra have been determined in 0.01 to 1 MHz range. The Nyquist curves fitting was achieved by using the equivalent circuit $R_1$, $R_2$, $R_3$, CPE1, and CPE2, in which $R_1$ denotes ohmic resistance or electrolyte's ohmic resistance, sum of $R_2$ and $R_3$ denotes electrode polarization resistance, and CPE1 and CPE2 are constant phase elements [46]. It was found that good performing cell (30ADC) produced lowest values of electrode polarization resistance and ohmic resistance of any other composition after conducting EIS under fuel cell conditions. This is demonstrated in Table 2. At 500°C, 30ADC produced an electrode polarization resistance of 0.40 Ω·cm$^2$ and an ohmic resistance of 0.13 Ω·cm$^2$. EIS spectra expose reduced resistance values, which offer additional indication for 30ADC electrolyte's efficient and well-behaved electrochemical properties in the fuel cell system. Correspondingly, at 550°C, pure ceria oxide produced ohmic resistance of 0.25 Ω·cm$^2$ [2]. The highest ionic conductivity in a desirable composition, which leads to rapid catalytic processes, is reflected in the least ohmic resistance. Increased compatibility between the electrolyte and electrode can help to improve fast ORR catalytic abilities, as seen by the decrease in electrode polarization resistance in 30ADC along with the ohmic resistance. Additionally, EIS of 30ADC cell was performed in the 380–500°C temperature range as displayed in Fig. 5(b). With the decrease of temperature, ohmic and polarization resistances increasing gradually, which also affected the conductivity and fuel cell performance.

As seen in Fig. 5(c), additional DRT analysis was conducted to examine the specific polarization dynamics of the Al–$CeO_2$ electrolyte using NCAL electrodes. The DRT curves exhibit four distinct peaks, denoted as P1–P4, ranging from high frequency to low frequency, signifying the presence of four primary processes that determine rate. A lower frequency, typically related to the polarization process from charge transfer, dissociative adsorption, or species surface exchange, to gas diffusion, is observed. On the other hand, a high frequency region is associated with the several phenomenon related to hydrogen adsorption, dissociation, proton formation, and lattice incorporation [47]. The $O_2$ adsorption/dissociation and oxygen species diffusion at the cathode side are shown by the P2 and P3 peaks, respectively. The $O^{2-}$ incorporation and transfer in the lattice can be attributed to

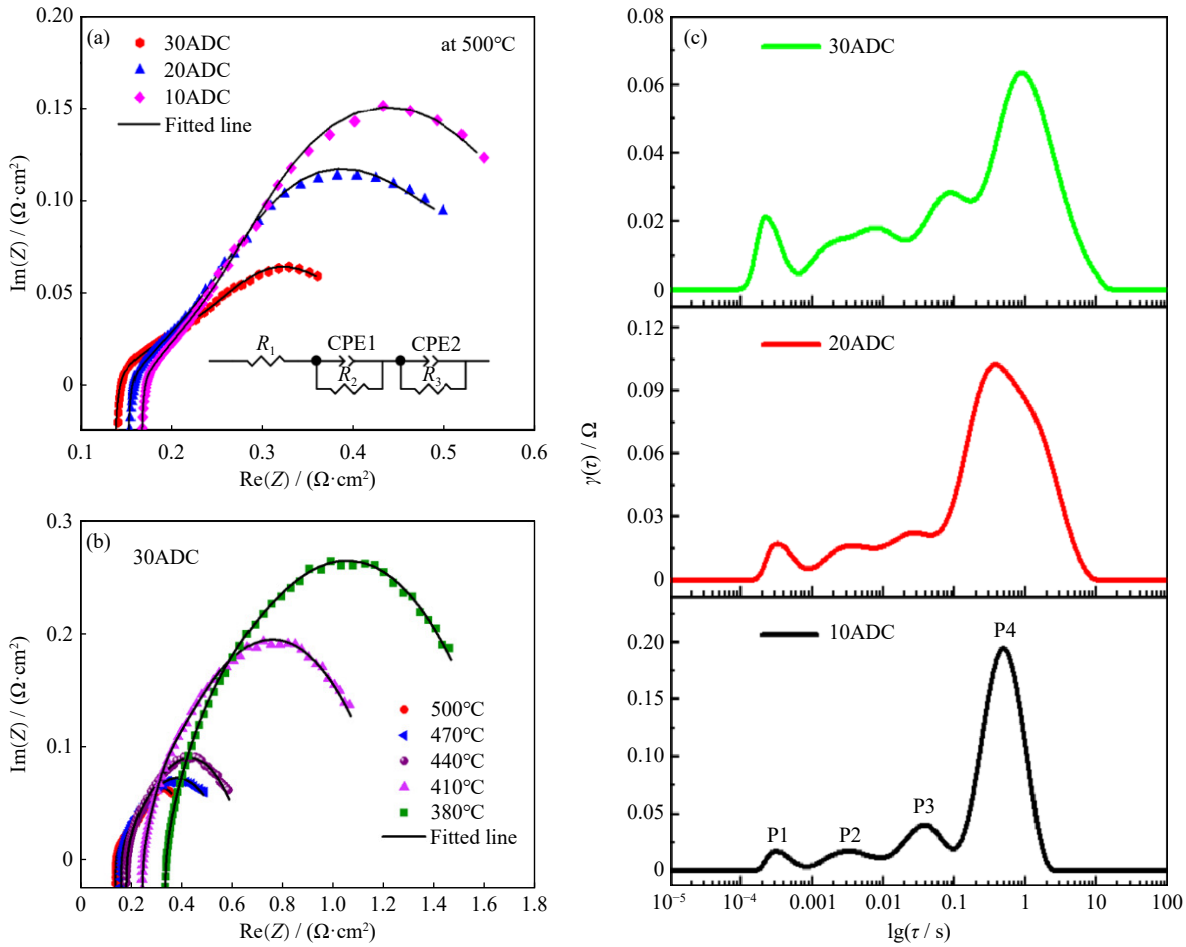


**Fig. 5. (a) EIS analysis comparison of 10ADC, 20ADC, and 30ADC at 500°C; (b) EIS analysis of 30ADC at different operational temperatures (380–500°C); (c) DRT analysis of Al–$CeO_2$ samples ($\tau$ is time constant and $\gamma(\tau)$ is a function of time constant).**

**Table 2. EIS comparison of fitting parameters, total conductivity ($\sigma_t$) from EIS, and ionic conductivity ($\sigma_i$) by *I–V* curves results at 500°C**

| Composition | $R_1$ / (Ω·cm²) | $R_2$ / (Ω·cm²) | $R_3$ / (Ω·cm²) | $\sigma_t$ (by EIS ) / (S·cm$^{-1}$) | $\sigma_i$ (by *I–V*) / (S·cm$^{-1}$) |
|---|---|---|---|---|---|
| 10ADC | 0.17 | 0.09 | 0.54 | 0.13 | 0.10 |
| 20ADC | 0.15 | 0.06 | 0.49 | 0.15 | 0.12 |
| 30ADC | 0.13 | 0.04 | 0.36 | 0.18 | 0.15 |

the peaks that exist as P1 and P2 in Al–$CeO_2$ [48]. Across all Al–$CeO_2$ samples, the P3 peak indicates the quickest reactions involving oxygen species in the sample. The material for PCFCs had much improved proton conductivity as a result of these treatments. Incorporating low valency cations, such as $Al^{3+}$, into $CeO_2$ produces a lattice strain that facilitates the creation of oxygen vacancies, hence enhancing the ionic conductivity overall.

There is no discernible difference in P1 intensity across all cells. If we compare 30ADC to other samples, it is interesting to note that the P4 peak with the lowest strength at low frequency appears there. Improved compatibility between electrolyte materials and cathode sample is demonstrated by the reduction of both ohmic resistance and electrode polarization resistance in 30ADC. This can help improve both the fuel cell performance and the quick ORR catalytic functions. The formation of P4 peak explained gas diffusion in the NCAL support electrode. At 500°C, the P4 of a cell based on 30ADC is the smallest and contributes the least amount of polarization. However, because the rate-limiting process only contributes a small amount to the continuous electrode polarization, its effect on the performance of the cell is minimal. This view acts as a catalyst for proton transport and produces local concentration gradients that raise the oxygen vacancy concentration, while also significantly improve Al–$CeO_2$ proton conductivity.

### 3.6. Ionic conductivity analysis and conduction mechanism

The ionic conductivity ($\sigma_i$) collected from the Fig. 4(a) and total conductivity ($\sigma_t$) collected from Fig. 5(b) of 30ADC are attained from the slope of polarization curves and EIS, as shown in Fig. 6(a). The ionic conductivity is acquired from 0.15 to 0.02 S/cm in temperature range of 380–500°C. The $\sigma_t$ collected by EIS reasonably exhibits high range of 0.18 to 0.06 S/cm in the same temperature range (380–500°C). It is reported that pure $CeO_2$ carried a conductivity of 0.052 S/cm at 550°C [39]. Upon incorporating Al into $CeO_2$,

an ionic conductivity of up to 0.15 S/cm at 500°C was achieved. Such a high ionic conductivity progresses fuel cell performance of electrolytes in PCFCs, smoothing the charge carrier movement. The enhanced conductivity is a consequence of increased ion mobilities in the ADC electrolytes as well as increase number of oxygen vacancies, as distinguished in XPS O 1s spectra as shown in Fig. 3(b). A noticeable improvement of conductivity in ADC electrolyte grasps remarkable potential for significantly enhancing the electrochemical performance of the fuel cells by employing such an electrolyte layer. 30ADC electrolyte's increased conductivity allows for more effective ion transport, accelerating reaction kinetics and lowering ohmic losses in the device. An increase in conductivity results in an increase in a device's power output, overall efficiency, and stability. The achieved ionic conductivity is noticeably higher than that of the proton conductor $Ba(Zr_{0.1}Ce_{0.7}Y_{0.2})O_{3-\delta}$ (BCZY) 0.02 S/cm at 700°C, the predominant oxygen ion conductor samarium doped ceria (SDC) ~0.05 S/cm at 700°C, the GDC 0.04 S/cm at 700°C, the ceramic YSZ 0.13 S/cm at 1000°C, and the GDC/YSZ mixture film ~0.01 S/cm at 1000°C [49–53].

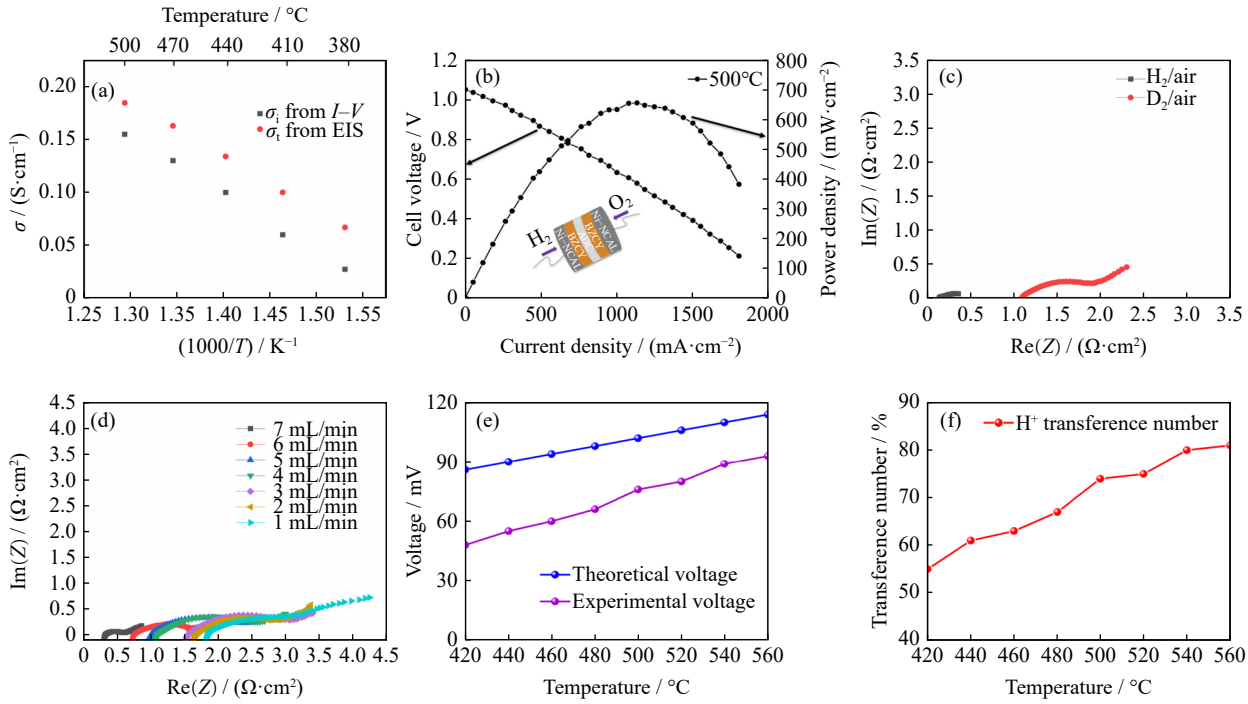


**Fig. 6. (a) Ionic conductivity from *I–V* curves and total conductivity from EIS at 380–500°C; (b) *I–P* and *I–V* characteristic curves of the oxygen ion blocking inserted fuel cell; (c) EIS spectra of 30ADC measured in $H_2$/air and $D_2$/air; (d) EIS spectra of 30ADC measured in different water partial pressure. (e) Theoretical and observed voltage of hydrogen concentration cell and (f) proton transport number during hydrogen concentration cell.**

To verify the core charge carriers in the fuel cell, an oxygen ion blocking layer by using well known proton conductor BZCY with preparation of NCAL–Ni/BZCY/30ADC/BZCY/NCAL–Ni was designed and tested. It permits only the transportation of protons and prevents the passage of oxygen ions via the electrolyte [54]. By eliminating the influence of other carriers, this blocking cell method has been used in prior investigations to assess a precise ionic conductivity [14,55–56]. This layer exclusively facilitates the transportation of $H^+$ ions and prevents the passage of $e^-/O^{2-}$ through the electrolyte membrane. Consequently, the current–voltage curve depicted confirms the transport of $H^+$ ions in 30ADC, establishing the dominant proton conduction in our device (Fig. 6(b)). The device exhibits a noteworthy OCV of 1.09 V and maximum power density of 656 mW/cm$^2$. Up to 75% of the fuel cell performance was achieved with BZCY layers as compared to without the BZCY layered cell. The additional interfaces introduced by the BZCY in the cell structure causes power losses at these interfaces, resulting in a 25% decrease in the output.

To further verifying the proton transport phenomenon in ADC materials, isotopic measurements were carried out. The 30ADC based fuel cell displays a clear difference in different atmosphere such as $H_2$ and $D_2$ as represented in Fig. 6(c). The big difference between D and $^1$H specifies an isotope effect, i.e., proton conduction in 30ADC. When $D^+$ and $H^+$ are integrated in 30ADC to form deuteroxyl/hydro groups ($OD^-$ or $OH^-$), protons and deuteroxyl/hydro groups migrate at a higher rate than deuterons, significantly exhibited in ohmic and polarization resistances.

Additionally, a fuel cell with the configuration of Ni–NCAL/30ADC/Ni–NCAL was fabricated to confirm the proton conduction by utilizing water with different partial pressure as a fuel. It was observed that by increasing water amounts, ohmic and polarization resistances decreased, as described in Fig. 6(d), which confirmed that more proton ($H^+$) and ($OH^-$) ions are moving through the membrane.

Hydrogen concentration cells and oxygen concentration cells were built in order to ascertain the conduction mechanism for 30ADC under fuel cell operating circumstances. By

using the predicted theoretical voltage and the actual voltage, the $H^+$ transference number was about 55%–81% between 420 and 560°C, as shown in Fig. 6(e) and (f). In the oxygen concentration cell test, no voltage was seen, and the oxygen ion transference number is 0 between 420 and 560°C. The measurements of concentration cells revealed that the 30ADC electrolyte was mainly proton conducting properties during fuel cells operation, with almost negligible oxygen ion conduction.

## 4. Conclusions

$Al^{3+}$ doping in $CeO_2$ possesses great potential for increasing oxygen vacancy concentration and creating surface and bulk gradience through careful control of the doping approach. These modifications significantly advanced the proton conductivity of the material for PCFCs. By systematically incorporating low-valency cations, such as $Al^{3+}$, into $CeO_2$, the resulting lattice strain promotes the formation of oxygen vacancies, thereby improving the overall ionic conductivity. Doping $CeO_2$ with $Al^{3+}$ ions offer an intriguing approach to inducing oxygen vacancies both in the bulk structure and on the particle surfaces. By substituting $Ce^{4+}$ with $Al^{3+}$ in varying proportions (10mol%, 20mol%, and 30mol%), the crystal lattice structure of $CeO_2$ is modified.

Additionally, by establishing doping gradients on the surface and in the bulk, local structural distortion and lattice strain are introduced, further promoting the uneven distribution of oxygen vacancies. This approach generates local concentration gradients that increase the concentration of oxygen vacancies and provide a driving force for proton transport, effectively enhancing the proton conductivity of Al-doped $CeO_2$. It was evidenced that introducing $Al^{3+}$ ions into $CeO_2$ significantly impacts its proton conductivity. The increased oxygen vacancy concentration results in a higher density of mobile charge carriers (protons) within the material. Furthermore, the surface and bulk doping gradients create local concentration driving forces that promote proton transport. Consequently, the overall ionic conductivity of Al-doped $CeO_2$ is greatly improved, enabling more efficient proton transport across the electrolyte. This enhancement in proton conductivity is vital for the performance of PCFCs, as it directly influences their power density and overall efficiency.

## Acknowledgements

This work was supported by the National Natural Science Foundation of China (Nos. 51772080 and 11604088), the Funding from Science and Technology Department of Jiangsu Province, China (No. BE2022029), and the Beijing Natural Science Foundation, China (No. IS23050). Prof. Asghar also thanks the Academy of Finland (Nos. 13322738 and 13352669) for the financial support.

## Conflict of Interest

The authors declare that there are no conflicts of interest regarding the publication of this paper.

## References

[1] F.Y. Liang, J.R. Yang, H.Q. Wang, and J.W. Wu, Fabrication of $Gd_2O_3$-doped $CeO_2$ thin films through DC reactive sputtering and their application in solid oxide fuel cells, *Int. J. Miner. Metall. Mater.*, 30(2023), No. 6, p. 1190.

[2] X. Yang, Z.H. Du, Q. Zhang, *et al.*, Effects of operating conditions on the performance degradation and anode microstructure evolution of anode-supported solid oxide fuel cells, *Int. J. Miner. Metall. Mater.*, 30(2023), No. 6, p. 1181.

[3] C.C. Duan, J.H. Tong, M. Shang, *et al.*, Readily processed protonic ceramic fuel cells with high performance at low temperatures, *Science*, 349(2015), No. 6254, p. 1321.

[4] H.P. Ding, W. Wu, C. Jiang, *et al.*, Self-sustainable protonic ceramic electrochemical cells using a triple conducting electrode for hydrogen and power production, *Nat. Commun.*, 11(2020), No. 1, art. No. 1907.

[5] X. Zhang, Y.K. Li, W. Zhao, J.X. Guo, P.F. Yin, and T. Ling, Technical factors affecting the performance of anion exchange membrane water electrolyzer, *Int. J. Miner. Metall. Mater.*, 30(2023), No. 11, p. 2259.

[6] S. Han, T. Wei, S.J. Wang, *et al.*, Recent progresses in the development of tubular segmented-in-series solid oxide fuel cells: Experimental and numerical study, *Int. J. Miner. Metall. Mater.*, 31(2024), No. 3, p. 427.

[7] T. Norby and A. Magrasó, On the development of proton ceramic fuel cells based on Ca-doped $LaNbO_4$ as electrolyte, *J. Power Sources*, 282(2015), p. 28.

[8] Y. Zhou, X.F. Guan, H. Zhou, *et al.*, Strongly correlated perovskite fuel cells, *Nature*, 534(2016), No. 7606, p. 231.

[9] Y.M. Xing, Y. Wu, L.Y. Li, *et al.*, Proton shuttles in $CeO_2/CeO_{2-\delta}$ core–shell structure, *ACS Energy Lett.*, 4(2019), No. 11, p. 2601.

[10] Y.Y. Liu, L.D. Fan, Y.X. Cai, W. Zhang, B.Y. Wang, and B. Zhu, Superionic conductivity of $Sm^{3+}$, $Pr^{3+}$, and $Nd^{3+}$ triple-doped ceria through bulk and surface two-step doping approach, *ACS Appl. Mater. Interfaces*, 9(2017), No. 28, p. 23614.

[11] S. Choi, C.J. Kucharczyk, Y.G. Liang, *et al.*, Exceptional power density and stability at intermediate temperatures in protonic ceramic fuel cells, *Nat. Energy*, 3(2018), p. 202.

[12] C.M. Li, Y.W. Zeng, Z.T. Wang, Z.P. Ye, and Y. Zhang, Processing temperature tuned interfacial microstructure and protonic and oxide ionic conductivities of well-sintered $Sm_{0.2}Ce_{0.8}O_{1.9}$–$Na_2CO_3$ nanocomposite electrolytes for intermediate temperature solid oxide fuel cells, *J. Power Sources*, 360(2017), p. 114.

[13] B.Y. Wang, B. Zhu, S.N. Yun, *et al.*, Fast ionic conduction in semiconductor $CeO_{2-\delta}$ electrolyte fuel cells, *NPG Asia Mater.*, 11(2019), art. No. 51.

[14] G. Chen, W.K. Sun, Y.D. Luo, *et al.*, Advanced fuel cell based on new nanocrystalline structure $Gd_{0.1}Ce_{0.9}O_2$ electrolyte, *ACS Appl. Mater. Interfaces*, 11(2019), No. 11, p. 10642.

[15] M.A.K.Y. Shah, Y.Z. Lu, N. Mushtaq, *et al.*, Designing Gadolinium-doped ceria electrolyte for low temperature electrochemical energy conversion, *Int. J. Hydrogen Energy*, 48(2023), No. 37, p. 14000.

[16] G. Chen, W.K. Sun, Y.D. Luo, *et al.*, Investigation of layered $Ni_{0.8}Co_{0.15}Al_{0.05}LiO_2$ in electrode for low-temperature solid oxide fuel cells, *Int. J. Hydrogen Energy*, 43(2018), No. 1, p. 417.

[17] J.J. Liu, F. Yang, Z. Jiang, *et al.*, Enhanced ionic conductivity and durability of novel solid oxide fuel cells by constructing a heterojunction based on transition and rare earth metal Co-doped ceria, *ACS Appl. Energy Mater.*, 4(2021), No. 12, p. 13492.

[18] C.Y. Kang, H. Kusaba, H. Yahiro, K. Sasaki, and Y. Teraoka, Preparation, characterization and electrical property of Mn-doped ceria-based oxides, *Solid State Ionics*, 177(2006), No. 19-25, p. 1799.

[19] C. Alvarez-Galvan, J.L. Martínez, M. Capel-Sanchez, L. Pascual, and J.A. Alonso, Magnetic properties of efficient catalysts

based on La-doped ceria-supported nickel nanoparticles for rWGS reaction. influence of Ni loading, *Adv. Sustainable Syst.*, 5(2021), No. 11, art. No. 2100029.
[20] E. Sartoretti, C. Novara, A. Chiodoni, *et al*., Nanostructured ceria-based catalysts doped with La and Nd: How acid-base sites and redox properties determine the oxidation mechanisms, *Catal. Today*, 390(2022), p. 117.
[21] H. Knözinger and P. Ratnasamy, Catalytic aluminas: Surface models and characterization of surface sites, *Catal. Rev.*, 17(1978), No. 1, p. 31.
[22] J. Sánchez-Valente, X. Bokhimi, and F. Hernández, Physicochemical and catalytic properties of sol–gel aluminas aged under hydrothermal conditions, *Langmuir*, 19(2003), No. 9, p. 3583.
[23] K. Jirátová and L. Beránek, Properties of modified aluminas, *Appl. Catal.*, 2(1982), No. 3, p. 125.
[24] T. Asada, T. Kayama, H. Kusaba, H. Einaga, and Y. Teraoka, Preparation of alumina-supported $LaFeO_3$ catalysts and their catalytic activity for propane combustion, *Catal. Today*, 139(2008), No. 1-2, p. 37.
[25] M.A.K. Y. Shah, Y.Z. Lu, N. Mushtaq, M. Yousaf, and B. Zhu, Doped ceria electrolyte rich in oxygen vacancies for boosting the fuel cell performance of LT-CFCs, *Int. J. Hydrogen Energy*, 48(2023), No. 33, p. 12474.
[26] S. Anirban, T. Paul, P.T. Das, T.K. Nath, and A. Dutta, Microstructure and electrical relaxation studies of chemically derived Gd–Nd co-doped nanocrystalline ceria electrolytes, *Solid State Ionics*, 270(2015), p. 73.
[27] M. Kahlaoui, A. Inoubli, S. Chefi, *et al*., Structural, chemical, and electrochemical properties of co-doped fluorite oxides $Ce_{0.8}La_{0.2-x}Tl_xO_{2-\delta}$ as electrolyte materials for solid oxide fuel cells, *Int. J. Hydrogen Energy*, 41(2016), No. 8, p. 4751.
[28] Z.T. Wang, Y.W. Zeng, C.M. Li, Z.P. Ye, L.L. Cao, and Y. Zhang, Structures and electrical conductivities of $Gd^{3+}$ and $Fe^{3+}$ co-doped cerium oxide electrolytes sintered at low temperature for ILT-SOFCs, *Ceram. Int.*, 44(2018), No. 9, p. 10328.
[29] Z.L. Wu, M.J. Li, J. Howe, H.M. Meyer, III, and S.H. Overbury, Probing defect sites on $CeO_2$ nanocrystals with well-defined surface planes by Raman spectroscopy and $O_2$ adsorption, *Langmuir*, 26(2010), No. 21, p. 16595.
[30] S. Anirban and A. Dutta, Revisiting ionic conductivity of rare earth doped ceria: Dependency on different factors, *Int. J. Hydrogen Energy*, 45(2020), No. 46, p. 25139.
[31] R. Schmitt, A. Nenning, O. Kraynis, *et al*., A review of defect structure and chemistry in ceria and its solid solutions, *Chem. Soc. Rev.*, 49(2020), No. 2, p. 554.
[32] Y.C. Wu and C.C. Lin, The microstructures and property analysis of aliovalent cations ($Sm^{3+}$, $Mg^{2+}$, $Ca^{2+}$, $Sr^{2+}$, $Ba^{2+}$) co-doped ceria-base electrolytes after an aging treatment, *Int. J. Hydrogen Energy*, 39(2014), No. 15, p. 7988.
[33] I. Kosacki, T. Suzuki, H.U. Anderson, and P. Colomban, Raman scattering and lattice defects in nanocrystalline $CeO_2$ thin films, *Solid State Ionics*, 149(2002), No. 1-2, p. 99.
[34] A. Mineshige, T. Taji, Y. Muroi, *et al*., Oxygen chemical potential variation in ceria-based solid oxide fuel cells determined by Raman spectroscopy, *Solid State Ionics*, 135(2000), No. 1-4, p. 481.
[35] S.A. Ansari, M.M. Khan, M.O. Ansari, S. Kalathil, J. Lee, and M.H. Cho, Band gap engineering of $CeO_2$ nanostructure using an electrochemically active biofilm for visible light applications, *RSC Adv.*, 4(2014), No. 32, p. 16782.
[36] X.Y. Zhang, J.Q. Qin, Y.N. Xue, *et al*., Effect of aspect ratio and surface defects on the photocatalytic activity of ZnO nanorods, *Sci. Rep.*, 4(2014), art. No. 4596.
[37] S. Sonsupap, P. Kidkhunthod, N. Chanlek, S. Pinitsoontorn, and S. Maensiri, Fabrication, structure, and magnetic properties of electrospun $Ce_{0.96}Fe_{0.04}O_2$ nanofibers, *Appl. Surf. Sci.*, 380(2016), p. 16.
[38] M. Caglar and F. Yakuphanoglu, Structural and optical properties of copper doped ZnO films derived by sol–gel, *Appl. Surf. Sci.*, 258(2012), No. 7, p. 3039.
[39] N. Shaheen, Z. Chen, M. Alomar, *et al*., Enabling fast ionic transport in $CeO_2$–$La_{1-2x}Ba_xBi_xFeO_3$ nanocomposite electrolyte for low temperature solid oxide fuel cell application, *RSC Adv.*, 13(2023), No. 30, p. 20663.
[40] M. Yousaf, Y.Z. Lu, E.Y. Hu, *et al*., Interfacial disordering and heterojunction enabling fast proton conduction, *Small Methods*, 7(2023), No. 9, art. No. 2300450.
[41] J.M. Zheng, H. Zhu, W.Q. Li, *et al*., Numerical study on the electron-blocking effect and optimized operation parameters of ceria-SOFCs with the pure Sm doping $CeO_2$ electrolyte, *Int. J. Hydrogen Energy*, 46(2021), No. 24, p. 13318.
[42] T. Mori, J. Drennan, J.H. Lee, J.G. Li, and T. Ikegami, Oxide ionic conductivity and microstructures of Sm- or La-doped $CeO_2$-based systems, *Solid State Ionics*, 154-155(2002), p. 461.
[43] S.F. Wang, Y.L. Liao, Y.F. Hsu, and P. Jasinski, Effects of $LiNi_{0.8}Co_{0.15}Al_{0.05}O_2$ electrodes on the conduction mechanism of $Sm_{0.2}Ce_{0.8}O_{2-\delta}$ electrolyte and performance of low-temperature solid oxide fuel cells, *J. Power Sources*, 546(2022), p. 231995.
[44] X.Z. Peng, Y.F. Tian, Y. Liu, *et al*., A double perovskite decorated carbon-tolerant redox electrode for symmetrical SOFC, *Int. J. Hydrogen Energy*, 45(2020), No. 28, p. 14461.
[45] X.M. Zhou and F. Zhou, Application of $La_{0.3}Sr_{0.7}Fe_{0.7}Ti_{0.3}O_{3-\delta}$/GDC electrolyte in LT-SOFC, *Int. J. Hydrogen Energy*, 46(2021), No. 15, p. 9988.
[46] Y.J. Meng, W. Zhang, Z.L. He, *et al*., Partially reduced $Ni_{0.8}Co_{0.15}Al_{0.05}LiO_{2-\delta}$ for low-temperature SOFC cathode, *Int. J. Hydrogen Energy*, 46(2021), No. 15, p. 9874.
[47] N. Shi, F. Su, D.M. Huan, *et al*., Performance and DRT analysis of P-SOFCs fabricated using new phase inversion combined tape casting technology, *J. Mater. Chem. A*, 5(2017), No. 37, p. 19664.
[48] A. Oz, K. Singh, D. Gelman, V. Thangadurai, and Y. Tsur, Understanding of oxygen reduction reaction on perovskite-type $Ba_{0.5}Sr_{0.5}Fe_{0.91}Al_{0.09}O_{3-\delta}$ and $Ba_{0.5}Sr_{0.5}Fe_{0.8}Cu_{0.2}O_{3-\delta}$ using AC impedance spectroscopy genetic programming, *J. Phys. Chem. C*, 122(2018), No. 27, p. 15097.
[49] I. Garbayo, D. Pla, A. Morata, L. Fonseca, N. Sabaté, and A. Tarancón, Full ceramic micro solid oxide fuel cells: Towards more reliable MEMS power generators operating at high temperatures, *Energy Environ. Sci.*, 7(2014), No. 11, p. 3617.
[50] N. Mahato, A. Banerjee, A. Gupta, S. Omar, and K. Balani, Progress in material selection for solid oxide fuel cell technology: A review, *Prog. Mater. Sci.*, 72(2015), p. 141.
[51] K. Prabhakaran, M.O. Beigh, J. Lakra, N.M. Gokhale, and S.C. Sharma, Characteristics of 8mol% yttria stabilized zirconia powder prepared by spray drying process, *J. Mater. Process. Technol.*, 189(2007), No. 1-3, p. 178.
[52] E. Fabbri, A. D'Epifanio, E.D. Bartolomeo, S. Licoccia, and E. Traversa, Tailoring the chemical stability of $Ba(Ce_{0.8-x}Zr_x)Y_{0.2}O_{3-\delta}$ protonic conductors for intermediate temperature solid oxide fuel cells (IT-SOFCs), *Solid State Ionics*, 179(2008), No. 15-16, p. 558.
[53] C. Zuo, S. Zha, M. Liu, M. Hatano, and M. Uchiyama, $Ba(Zr_{0.1}Ce_{0.7}Y_{0.2})O_{3-\delta}$ as an electrolyte for low-temperature solid-oxide fuel cells, *Adv. Mater.*, 18(2006), No. 24, p. 3318.
[54] M.A.K.Y. Shah, Y.Z. Lu, N. Mushtaq, *et al*., Perovskite Al–Sr-$TiO_3$ semiconductor electrolyte with superionic conduction in ceramic fuel cells, *Sustain. Energy Fuels*, 6(2022), No. 16, p. 3794.
[55] F.Z. Wang, E.Y. Hu, H. Wu, *et al*., Surface-engineered homostructure for enhancing proton transport, *Small Meth.*, 6(2022), No. 1, art. No. 2100901.
[56] D.A. Medvedev, J.G. Lyagaeva, E.V. Gorbova, A.K. Demin, and P. Tsiakaras, Advanced materials for SOFC application: Strategies for the development of highly conductive and stable solid oxide proton electrolytes, *Prog. Mater. Sci.*, 75(2016), p. 38.